



Measurement of Microscale Shear Forces during Chemical Mechanical Planarization

Robert D. White,^z Andrew J. Mueller, Minchul Shin, Douglas Gauthier,
Vincent P. Manno, and Chris B. Rogers

Tufts University, Medford, Massachusetts 02155, USA

Polydimethylsiloxane (PDMS) posts with a diameter of 80 μm were used to measure the shearing forces at the wafer-pad interface during chemical mechanical planarization (CMP). Measurements were made at 10 kHz with measurable forces between 40 and 400 μN . The structures were polished using a stiff, ungrooved pad and 3 wt % fumed silica slurry at velocities of 0.3 and 0.6 m/s and average wafer-pad normal load of 5.0 and 9.1 kPa. Due to the small fraction of the pad that contacts the wafer, the local microscale forces can be much larger than the global average force might suggest. Observed lateral forces on the structures averaged, in time, between 230 and 310 μN with RMS deviations of the force about the mean between 47 and 64 μN . The faster polishing case shows a 30% higher mean force, and a 20% reduction in the RMS variation of force. Little change is seen in the force characteristics when increasing from 5.0 to 9.1 kPa downforce. A mathematical model is developed to interpret these forces, allowing estimation of the local pad properties. The model suggests that 5000 asperity contacts are present per square millimeter, asperity lateral stiffness is 0.3 N/m, and asperity slip-off force is 19 μN .

© 2011 The Electrochemical Society. [DOI: 10.1149/1.3616021] All rights reserved.

Manuscript submitted March 30, 2011; revised manuscript received June 29, 2011. Published August 5, 2011.

Chemical Mechanical Planarization (CMP) is a critical process for semiconductor manufacturing. As feature sizes continue to shrink and depth of focus in the optical lithography systems decreases, planarity plays an increasingly important role in successful lithography. The CMP process is widely used to ensure planarity and, for certain systems, has been characterized experimentally in terms of many of the polishing parameters.^{1–4} Models of polish rate dependence on an important subset of the mechanical and chemical variables for certain polishing systems have been developed.^{5–7} Still, a comprehensive model involving the multitude of process variables and their effects on material removal rates, planarity, and defectivity remains elusive.

The development and validation of some aspects of this “total CMP model” is hindered by lack of knowledge of *in situ* shear forces present at the micro-scale. Polishing occurs at the micro- or nano-scale, at the size scale of either the pad asperities or the abrasive particles. The size scale of wafer features that are being polishing is also relevant. Therefore, experimental data of shear forces from single asperities (scales in the tens of microns) or below, is needed to understand the local phenomena that directly cause material removal to occur. In a direct sense, knowledge of the local shear forces may be important in designing fragile structures, such as low-k dielectrics or photoresist layers, to withstand polish. In addition, the development of *in situ* surface force sensors that can be used in the polishing environment may open up new possibilities for better in-process control, endpoint detection, and pad design.

Although a number of researchers have measured the global average shear force *in situ*,^{2,8–10} there is reason to think that the actual interaction forces present at the pad wafer interface are not well distributed, but are concentrated at relatively small points of contact. Research from our group^{11,12} and from other sources¹³ suggests that the pad-wafer contact percentage is on the order of 1% or below. Thus microscale forces at interaction regions are likely to be 100 times or more higher than a simple area average would suggest. It seems likely that these high local interaction forces are the ones responsible for both desirable polishing, as well as one source of defects produce during polishing, such as scratching and gouging of the surface.

The areas of contact are of variable geometry, but appear to often be on the order of 10–100 μm in size.^{11,13} Measurement of those local forces therefore requires sensor structures of the similar size. The sensor structures must also be able to withstand the polishing environment, provide high enough temporal information to capture single interaction events. Pad-wafer relative velocities are on the

order of 0.1–1 m/s. With 10–100 μm size structures, sample times on the order of 10 μs –1 ms will be required.

In this paper, we detail the fabrication, calibration, and deployment of micromachined shear stress sensors for characterizing these *in situ* local contact forces at the required spatial and temporal scales. While some research groups have investigated micro- or nano-scale interaction forces with relevance to CMP *ex situ*,^{14,15} the work described in this paper represents, to the best of our knowledge, the first attempt to measure local microscale polishing forces *in situ*. In addition, a novel dynamic model of contact is developed for this specific case and applied to extract local pad properties from measurements of the microscale polishing forces. It may be possible to connect these local pad contact properties to defectivity, planarity of the polish, and polishing rate in order to improve pad, slurry, and polishing tool designs.

Mechanical structure

The basic structure and function of the sensor is shown in Fig. 1. An individual sensor element consists of a single 80 μm diameter cylindrical PDMS post in a cylindrical well. An array of these posts is fabricated and bonded to a glass wafer, which is placed into the polishing setup and polished under normal polishing conditions. The top of the post is co-planar with the top of the well, so that the majority of the wafer surface is flat, and thus able to support the normal force of the pad pressing into the surface. The well extends 50 μm beyond the edge of the post in all directions. The post itself is 80 μm tall. As asperities on the pad contact the post, the contact force causes the post to bend. The structure is fully transparent so that the dynamic deflection of the post tops may be observed from the back of the wafer during polishing. By measuring the tip deflection optically from the backside, we are able to extract both the magnitude and the direction of the in-plane force. Polydimethylsiloxane (PDMS) was chosen for its low elastic modulus of approximately 750 kPa.¹⁶ This low modulus is needed in order to produce measurable deflections over the range of expected forces. We emphasize here that PDMS is a polymeric material that has a much lower modulus than silicon, silicon dioxide, and copper. It also tends to exhibit higher adhesive forces to the pad than these materials. Hence, the results shown in this paper are most applicable to the polishing of polymers (such as photoresists) and should be thought of as a step towards measurement of contact forces that may be present for the polishing of harder materials.

Three dimensional finite element modeling of the PDMS post structure was conducted to determine structure compliance. The mesh and boundary conditions are shown in Fig. 2. Symmetry

^z E-mail: r.white@tufts.edu

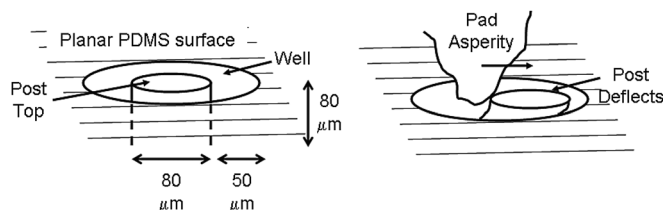


Figure 1. Diagram of the mechanical structure and geometry of the post-in-well sensor. In response to forcing by a passing pad asperity, the post tip deflects.

considerations require only half of the structure to be modeled. Fixed boundary conditions are applied on the bottom and sides of the base region. A distributed shear traction is applied to the top surface of the structure in the lateral direction.

It is important to include the compliance of the bulk PDMS below the post in order to correctly predict post tip deflection in response to a lateral shear force. AbaqusTM computer aided engineering software was used to perform the FEA simulation using C3D4H elements. These elements are four node linear tetrahedrons utilizing a hybrid displacement/pressure formulation. It is important to use a hybrid formulation due to the nearly incompressible material properties, which can result in element locking if a hybrid formulation is not used. An elastic modulus of either 750 kPa or 1.5 MPa (both results are reported) was used for the PDMS, and a Poisson ratio of 0.5. The 750 kPa value is chosen based on literature reports for untreated PDMS [e.g. (Ref. 16)] and agrees reasonably well with calibrated stiffness of the structure prior to oxygen plasma treatment. The 1.5 MPa value more closely matches the experimentally determined stiffness of the structure after oxygen plasma treatment. A mesh density convergence study was conducted to ensure the solution was converged. Nonlinear large deformation geometric effects were included in the computation.

Figure 2 shows the FEA mesh and the geometry, including the location of the back corner point. In Fig. 3, FEA model predictions for the lateral deflection of the back corner point are plotted versus total applied force to the post top. Since only half the structure is modeled, the force reported in all the results is twice the force applied to the computational model. This force can then be directly compared to experimental results. With a modulus of 750 kPa (1.5 MPa), the predicted small-deflection post compliance is 0.24 $\mu\text{m}/\mu\text{N}$ (0.12 $\mu\text{m}/\mu\text{N}$). At the maximum possible deflection of 50 μm (at which point the post will contact the edge of the “well” region), the stiffness nonlinearity is 4% for the 750 kPa material, and 2% for the 1.5 MPa material. These results are confirmed by experimental characterization discussed later in the paper.

These computations predict the expected static performance of the structure. However, the system will be used in a dynamic envi-

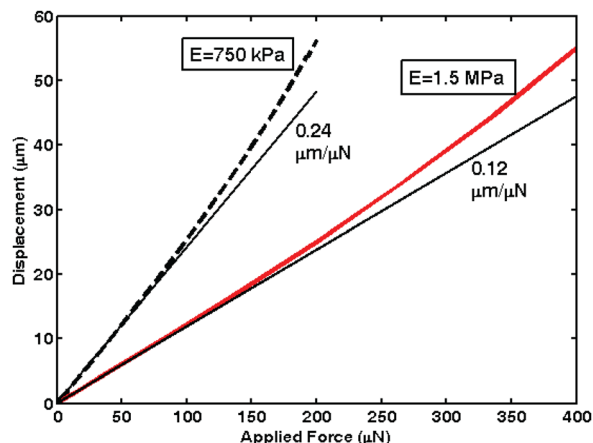


Figure 3. (Color online) Results of FEA computation – lateral deflection of the back corner point on the post in response to a distributed shear load on the top surface of the post. The dark dashed black line and dark solid red line are the FEA results for two different moduli, as indicated. The thinner black lines are a linear fit to the low deflection part of the curve.

ronment as it will be excited by potentially high frequency polishing forces. In order to estimate the first resonant frequency of the structure, the methods described by Kirstein, et al are used.¹⁷ Kirstein gives expressions for the effective added mass and damping produced by an infinite viscous incompressible fluid environment interacting with a circular beam. Although the fluid environment is, in this case, not infinite, the constraining effects of the shallow well are expected to produce only small corrections. The first *in vacuo* resonant frequency for the PDMS post is 38 kHz, computed using finite element methods for the same structure shown above with a modulus of $E = 1.5$ MPa, a Poisson ratio of 0.5, and density of $\rho = 970$ kg/m³. After adding the effective fluid mass and damping as described by Kirstein for a fluid with a density of 1000 kg/m³ and a viscosity of 0.0018 Pa·s,¹⁸ the predicted fluid loaded resonant frequency for the structure is 25 kHz. This is well above the Nyquist frequency of the measurements taken in this paper ($f_{Ny} = 5$ kHz), so the structure is expected to act in a quasistatic manner for measurable frequencies.

Expected forces during polishing

The post design is based off of estimates of shear forces present while polishing a 100 mm diameter wafer using an IC1000 pad with a static applied pressure of 12 kPa. This case is chosen due to the useful and unique confocal microscope results available from Elmufdi et al.¹³ Contact occurs over only approximately 0.7% of the wafer,¹³ resulting in a total contact area of 55 mm² for a 100 mm diameter wafer. In this same work, a confocal microscopy picture is

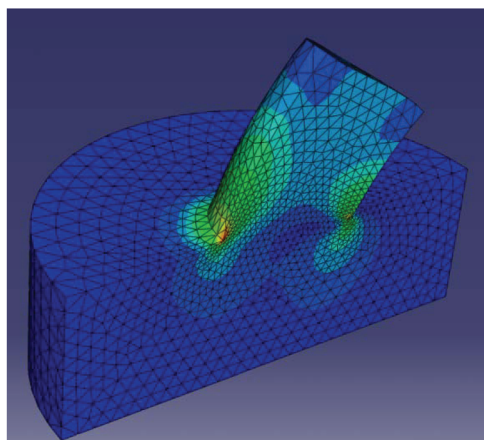
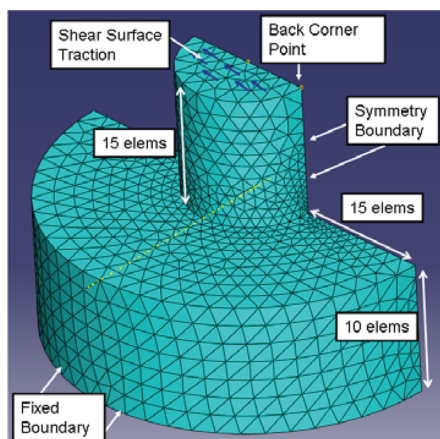


Figure 2. (Color online) Mesh, boundary conditions, and example result for the three dimensional finite element model of the post and base.

given showing the size and shape of contact areas. The size varies considerably, but a representative contact region appears to be approximately $1 \cdot 10^{-4} \text{ mm}^2$ in area. Dividing total contact area by the average size of the contact region, this suggests roughly 5.5×10^5 contact “points” are present at any given time. This is 70 contacts per square mm. For this same pad and downforce, a global average coefficient of friction (CoF) value of $0.30 (\pm 0.03)$ was measured during polishing by our group. The total shear force on the 100 mm diameter wafer at this downforce is thus approximately 28 N. On average, then, we expect contact point shear forces on the order of $50 \mu\text{N}$. This computation is conducted only to determine an order of magnitude expected level of asperity interaction force. The forces may extend considerably both above and below this average. We also emphasize here that this estimate of the number of contacts between the pad and wafer are approximate at best. The number of contacts needs further experimental investigation, which may be possible using the PDMS structure described in this work.

Forces will also be present on the structure from slurry flowing past the structure during polishing. Finite element computations have been carried out for this structure to produce an estimate of the order of magnitude of expected fluid forces. For the purposes of the fluid mechanics computation, the structure shown in Fig. 4 is used, with fluid filling the well and extending above the top of the post and PDMS surface. The structure is considered rigid for the purposes of this computation. The incompressible, linearized Navier Stokes equation is solved for the steady state flow using the properties of water: a density of 1000 kg/m^3 and a viscosity of $0.0018 \text{ Pa}\cdot\text{s}$. Measurements of fumed silica slurry viscosities over a range of particle loadings and shear rates can be found in Lortz, et al, and do not vary far from this value.¹⁸ An inflow boundary condition fixes the inlet fluid velocity along the boundary at $x = 0$. The top of the fluid film is fixed at the pad velocity, and the bottom of the fluid film has a velocity of zero. Initial linear (Couette) flow is assumed along the inlet boundary. No-slip walls are used for the structure. Symmetry conditions are used along both edges in the y-direction. The “pad” surface is on the top of the fluid film and is fixed at the pad velocity. The outlet surface has a pressure of zero, to allow all incoming fluid to escape with no internal static pressure increase. Figure 4 below shows the mesh and boundary conditions. P_2P_1 Lagrange elements are used in Comsol MultiphysicsTM to solve the problem. These elements are three dimensional tetrahedral elements with second order shape functions. A reduced integration scheme is used. A mesh density convergence study has been conducted to ensure that the solution is fully converged.

Results were computed at a pad velocity of 0.6 m/s , and fluid film thicknesses of 60 and $10 \mu\text{m}$. The pad velocity is chosen to match the experimental cases presented later in this work. It should be noted that this is a linearized computation, so the structural force is linear with applied velocity, so a result at any velocity is sufficient. The fluid film thicknesses were chosen based on the range of fluid film thicknesses measured by Gray, et al for glass polishing in the same experimental setup used here.^{11,19} The pad-wafer gap can

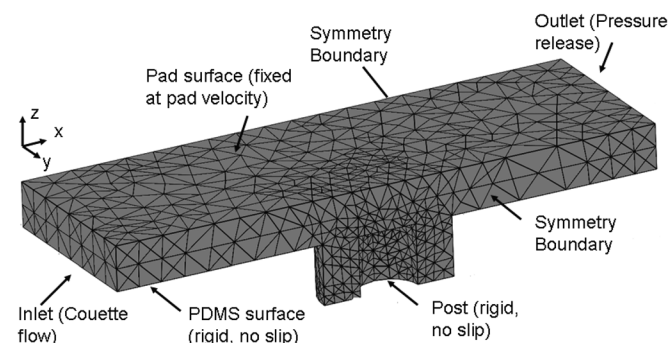


Figure 4. Fluid mesh and boundary conditions.

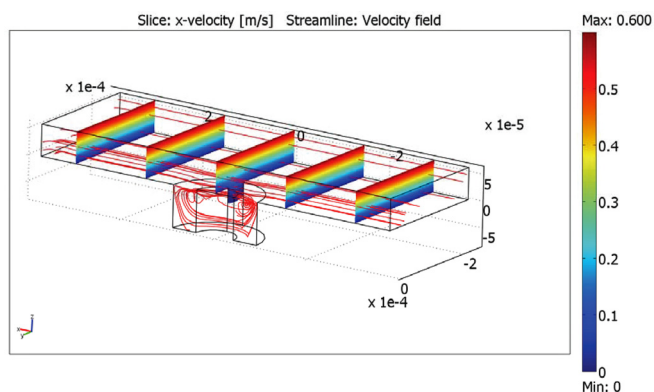


Figure 5. (Color online) Streamlines and x-direction velocity field for the 0.6 m/s pad velocity, $60 \mu\text{m}$ thick fluid film case.

go all the way to zero (when contact occurs) and may be larger than $60 \mu\text{m}$ in some cases; indeed, the exact value of the pad-wafer gap is variable and not well known. Nevertheless, 10 and $60 \mu\text{m}$ fall within the experimentally observed range, and will serve to give a sense of the magnitude of the fluid forces. The result of the computation for the $60 \mu\text{m}$ gap case, showing streamlines and x-direction fluid velocity, is given in Fig. 5. A strong region of recirculation is seen in the well around the post, with a three dimensional character. In the region above the post, Couette flow dominates.

The pressure and shear stress vary over both the top and side surfaces of the post. Integrating the total pressure and shear stress over the surface of the post, dotted with the x-direction unit vector, gives a total lateral resultant force on the structure. Since only half the structure is modeled, the total force is doubled to arrive at a total fluid force estimate. This force is not equivalent to a tip force, as it is distributed in a nonuniform manner over the surface of the post. However, since the post will exhibit maximum deflection for a force at the tip, the total lateral force on the structure, if applied at the tip, gives an upper bound to the deflection of the tip. The total lateral fluid force at $60 \mu\text{m}$ fluid film thickness is 86 nN , and at $10 \mu\text{m}$ fluid film thickness is 146 nN . Based on the estimated pad-wafer contact forces for single asperity contact ($50 \mu\text{N}$), fluid forces are expected to contribute only a very small fraction of the total lateral force.

Interestingly, at $60 \mu\text{m}$ fluid film thickness, the majority of the fluid forces on the post come from shear stresses on the top surface of the post, and the FEA result is very similar to what one would compute just assuming undisturbed Couette flow and multiplying the shear stress on the top of the post by the post top area

$$F \approx \frac{A\mu}{Vh} = \frac{\pi(40\mu\text{m})^2(0.0018\text{Pa}\cdot\text{s})}{(0.6\text{m/s})(60\mu\text{m})} = 90\text{nN} \quad [1]$$

where A is the post top area, μ is the fluid viscosity, V is the pad velocity, and h is the fluid film thickness. However, in the $10 \mu\text{m}$ thick fluid case, although the shear force on the top of the post increases due to the larger vertical velocity gradient, the pressure force in the recirculating region within the well also becomes larger and opposes the tip shearing force to a greater degree, thus resulting in considerably less lateral force than would be expected based on the shear on the post top.

Microfabrication

The structures were fabricated using a PDMS micromolding process similar to that described in Ref. 20. The mold is fabricated on a 100 mm diameter, $\langle 100 \rangle$ oriented silicon wafer with $1 \mu\text{m}$ of thermally grown surface oxide. SU-8-100 (MicroChem Corp.), a negative epoxide based high-aspect ratio photoresist, is spun on at $80 \mu\text{m}$ thickness to define the main features of the structure. Considerable process optimization of spin speeds, times, and bake parameters was

carried out to ensure uniform film thickness. The optimal parameters from this study were a 500 rpm spread for 30 s followed by a 3000 rpm spin for 70 s. Prebake was at 65°C for 15 minutes followed by 95°C for 32 min on two hotplates. Exposure was carried out using an OAI Model 204 contact aligner. The total exposure dose was 300 mJ/cm² at I-line, with an additional approximately 300 mJ/cm² at H-line and 300 mJ/cm² at G-line. It should be noted that only the I-line component of the lamp intensity is measured and controlled. The other two intensities are implied from manufacturer-supplied data on a typical mercury lamp spectrum. The post exposure bake was 65°C for 1 min followed by 95°C for 10 min. Develop time was 10 min in PM Acetate. This results in an 80 μ m thick film with a maximum variation of ± 5 μ m across the wafer, as measured using stylus profilometry.

After exposure and develop, the master mold surfaces are silanized by exposure to a tridecafluoro tetrahydroctyl trichlorosilane for 3 h in a vacuum desiccator under rough vacuum. This aids in releasing the PDMS from the mold later on, and allows the mold to be used for the production of multiple PDMS structures. Dow Corning Sylgard 184 base and curing agent is then mixed in a 10:1 ratio to produce the liquid PDMS which is degassed in a vacuum desiccator for 1 h and poured over the mold. The structure is then cured on a hotplate at 60°C for 4 h. A leveling table is used to ensure that the mold is level, creating a uniform PDMS thickness. After curing, the PDMS structure is peeled off of the mold.

A microscope picture is shown in Fig. 6. The compliant PDMS structure is bonded to a 0.5 mm thick Pyrex glass wafer (Corning type 7740 Pyrex glass) by exposing both surfaces to a 200 mT, 25 W oxygen plasma for 30 s, placing the PDMS and glass in contact, and heating on a hotplate at 60°C for 15 min. This Pyrex wafer gives a transparent rigid backplate to the structure. A 15 nm thick Chromium film is finally sputtered onto the front side of the PDMS to aid in image contrast, and the entire structure is bonded to a stiff aluminum backing plate using epoxy. The aluminum plate has windows machined in it for viewing through the backside, and includes mounting hardware for connecting to the polisher shaft.

Mechanical calibration

Post tip stiffness calibration was carried out using a microscale mechanical testing technique, called MAT-Test, developed by Hopcroft et al.²¹ The technique utilizes a contact surface profilometer to obtain force deflection curves for small structures. To determine the stiffness of the PDMS sensing posts, calibration posts were fabricated using an identical procedure, but were fabricated without the surrounding

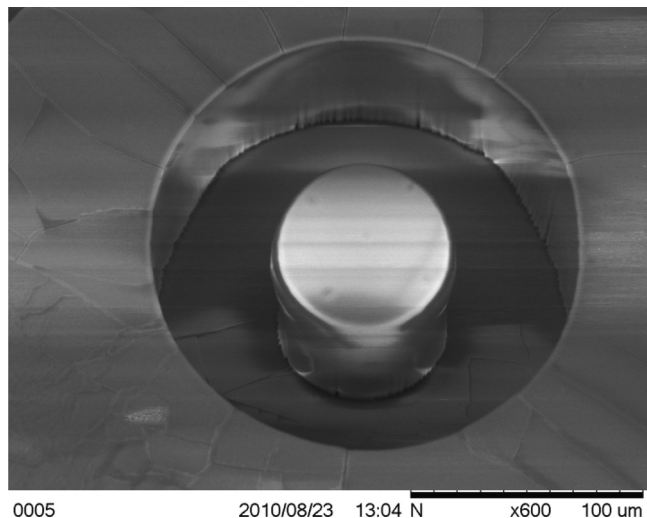


Figure 6. Scanning electron microscope image of the PDMS post after fabrication (before polishing). Some cracking of the Chromium thin film is visible.

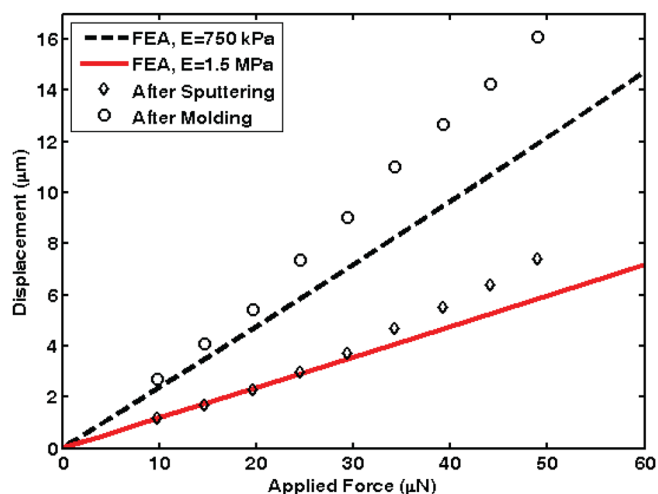


Figure 7. (Color online) Comparison of measured tip stiffness to expected stiffness as computed by FEA with two different moduli. The measured tip stiffness is given after molding, and then again after oxygen plasma treatment and sputtering.

“well”, in order to allow easy access to the side of the post. The PDMS was cut with a blade and oriented horizontally, so that the stylus tip could travel from the base to the tip of the post. By picking off the tip deflection at a series of different downforces, force vs. deflection curves were obtained. A Veeco Dektak 6M Stylus Profilometer was used to supply downforces between 10–50 μ N. Calibration runs were carried out after molding, and then again after oxygen plasma treatment and sputtering. Results are shown in Fig. 7. Before oxygen plasma treatment, the structure stiffness is similar to that predicted by FEA with a PDMS modulus value, taken from Ref. 16, of 750 kPa. However, as can be seen in the figure, the structure becomes approximately twice as stiff after oxygen plasma treatment and sputtering, agreeing closely with model predictions using a modulus of 1.5 MPa, for small deflections. The final small-deflection compliance of the post, as measured using this calibration method, is 0.12 μ m/ μ N. At an applied force of 50 μ N, the structure exhibits 3.2% nonlinearity. The structure measurements show more nonlinearity than predicted by the FEA model, suggesting that the nonlinearity may be due to material nonlinearities rather than geometric nonlinearities, as only geometric nonlinearities were captured by the computational model.

Optical measurement

During polishing, the tip displacement of the post must be inferred from optical measurements from the backside of the wafer. As shown in Fig. 8, an optical system consisting of a Phantom v7.0

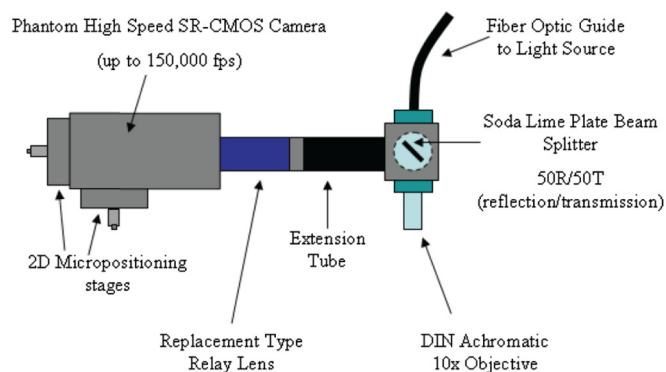


Figure 8. (Color online) Optical system for measuring post deflection through the wafer backside.

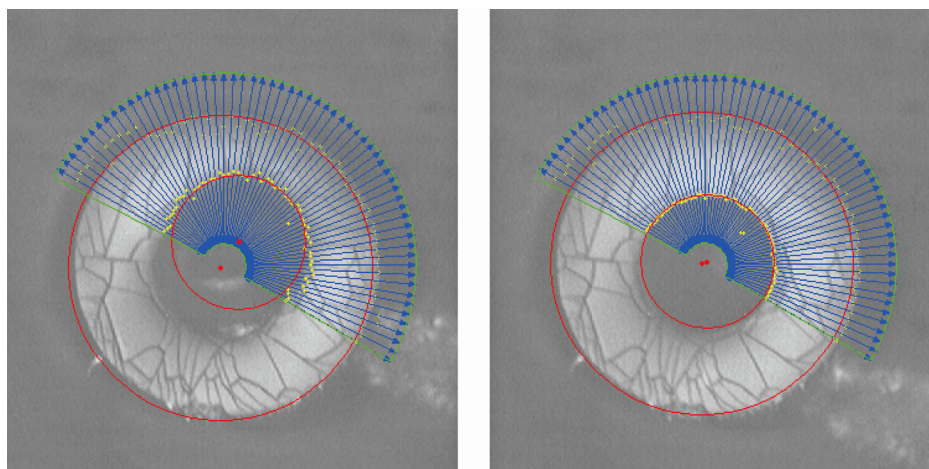


Figure 9. (Color online) Two example calibration images showing a deflected post (left) and an undeflected post (right).

high speed camera with a 12 bit SR-CMOS sensor coupled to a 15 X relay lens and a 10 X microscope objective is used to determine post deflection during CMP. Light is provided to the sensor through the microscope objective using a fiber optic light guide and 90° soda lime plate beam splitter. The system is mounted on a micropositioning stage for focusing and positioning. For all experiments described here, the camera resolution and speed are set at 512×384 pixels and 10,000 frames per second, respectively. At 10,000 frames per second, for a relative pad speed of 0.6 m/s, a point in the image moves $60 \mu\text{m}$ between one frame and the next. Hence, individual asperities spaced more than $60 \mu\text{m}$ apart should be resolved. Pixel size is $1.7 \mu\text{m}$, setting the minimum measurable force.

Image processing is performed in post processing on the recorded movies of post deflection to extract the relative motion of the post top. Edge detection finds points along the edge of the well and along a 180° segment along the leading edge of the post top. Two circles with fixed diameters ($180 \mu\text{m}$ for the “well”, $80 \mu\text{m}$ for the post) are fit to these points. The relative motion of the center of the circles gives the deflection of the post top relative to the fixed “well” in two dimensions. Two example images are shown in Fig. 9. Image processing is carried out on the front half of the post (green region) to fit two circles to the post leading edge and the well (red circles). The identified centers of these two circles are shown by the red dots.

One final calibration step is needed in order to relate the image deflection, as measured using the method described above, to actual deflection of the post tip. It is not clear that the elongated shadow seen in the deflected image (for example, in Fig. 9) is in fact the front edge of the post tip. It is quite possible that this is, in fact, a shadowed region created by deformation of the Chromium film near the base of the post. In addition, the images processing algorithm is tracking the motion of the front edge of the post, while forces are being applied to the back of the post. Thus, the motion of the image needs to be related to the actual deflection at the back of the post, which is related to applied force.

In order to investigate this, the PDMS structure was removed from the polishing setup and clamped onto an optical stage. A stiff probe tip needle was mounted on a 3D XYZ micropositioning stage (Newport 443 with LTA-HS actuator and closed loop computer control), and used to push the tip of the post over by a known increment. At each $5 \mu\text{m}$ increment, an image was captured from the backside using the same illumination scheme shown above, but using a still camera rather than the high speed Phantom camera. The same image processing code was then used to extract the apparent motion of the post top, and the result was compared to the actual motion of the stiff probe pushing on the back of the post. Figure 10 shows the results for both forward and backwards motion of the post (first pushed forward, then pushed backward). The result gives a good linear relationship between apparent and actual motion, with a small offset ($2.1 \mu\text{m}$) at zero deflection. The apparent motion is 36% of the actual motion.

With the force and optical calibration results in hand, the actual force experienced from the structure during polishing can now be extracted from image processing results on the high speed video. The magnitude of the applied force is

$$F = \frac{X}{(0.36)(0.12 \mu\text{m}/\mu\text{N})} \quad [2]$$

Experimental results

Polishing studies were conducted in a tabletop polisher (Struers RotoPol 31), shown in Fig. 11, using an ungrooved IC1000 pad (Rodell, Newark, Del.) without pad conditioning. A fumed silica slurry diluted to 3% by weight particle loading (Cabot Microelectronics, Aurora, IL) was used. We emphasize again that the surface of the substrate that is being polished is manufactured out of the low modulus polymer, polydimethylsiloxane (PDMS). This is likely to have a significant impact on the polishing forces, as compared to the polishing of stiffer materials such as glass or various metals. As is typical in CMP, the polishing pad is rotating during polishing. Typically in CMP the wafer would counter-rotate to improve polish uniformity. However, for these experiments, the wafer is *not* counter-rotating due to limitations with the optical setup. This implies that the polish may not be uniform across the wafer. In addition, previous work²² demonstrated a substantial

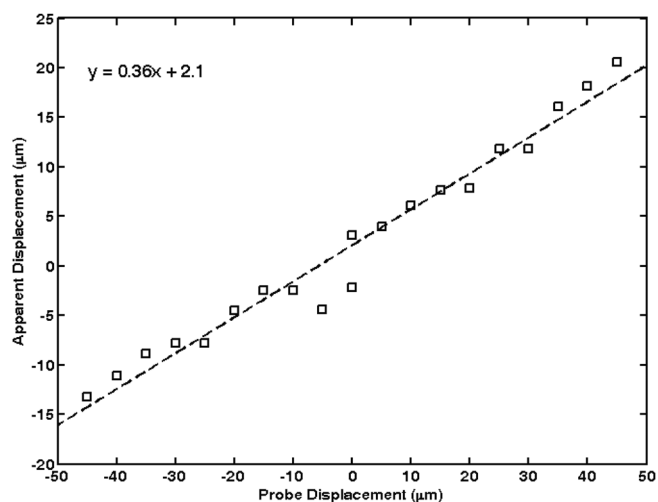


Figure 10. Deflection determined by the automated image processing method compared to the actual deflection of a stiff probe pushing the post tip laterally. Black squares are the measured data. The dashed black line is a linear fit.

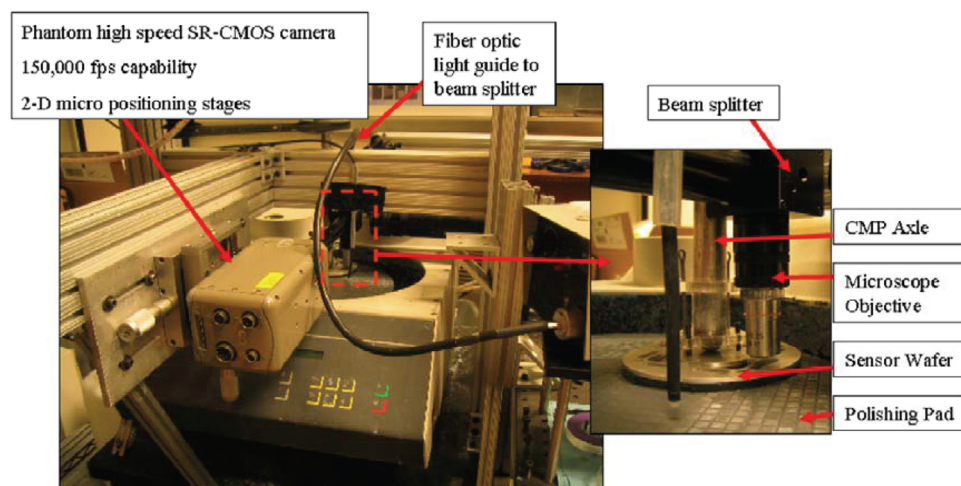


Figure 11. (Color online) Photograph of the polishing setup. (Left) The entire polisher with the mounted camera and frame. (Right) A closer view of the wafer being polished, along with the microscope objective and the slurry injection tube.

change in the pressure profile under the wafer due to wafer rotation, which may be altered in this case.

Measurements were conducted with applied normal pressures of 5.0 and 9.1 kPa. Two different rotation speeds, 30 and 60 rpm, were used for the polishing platen. The center of the wafer is approximately 10 cm from the center of rotation of the platen, hence 30 rpm corresponds to 0.3 m/s relative velocity, and 60 rpm corresponds to 0.6 m/s relative velocity.

The Chromium thin film on the top of the structures is polished away over the entire wafer, demonstrating that polishing is occurring. In addition, on the tip of the posts, the Chromium is polished from the leading edge of the post, but not from the back edge, indicating that the posts are also being polished, and that they are deflecting in response to pad interactions. No major degradation of the PDMS structure is observed, nor are substantial residues left on or around the post by the polishing process. Both of these observations are illustrated by the microscope images in Fig. 12.

Time traces of the results for the three cases are shown in Figs. 13–15. In all three cases, a substantial non-zero mean force on the order of 200–300 μN is observed in the direction of polish. The variation of the force around the mean is on the order of 50–60 μN_{rms} . Spectral analysis performed with a Hanning window, also shown in Fig. 13, reveals a $(1/f)^N$ behavior for the power spectral density (PSD). A least squares best fit for all data above 100 Hz gives N close to 1 for both the 0.3 m/s cases and $N=0.56$ for the 0.6 m/s case. Note that this would be a $(1/f)^{(N/2)}$ spectrum if the PSD were expressed in units of $\mu\text{N}/\sqrt{\text{Hz}}$. Table I summarizes the results for the three test cases. The two slower speed cases are not strikingly different. However the faster polishing case shows a 30% higher mean surface interaction force, a 20% reduction in the RMS variation of force about the mean, and a significant change in slope for

the PSD of the force. Note that the maximum measurable force for the system is 420 μN , at which point the post will touch the wall. For the majority of the measured time, the force is below this maximum, so saturation does not appear to be a limitation.

One common way to present the mean force data for contact experiments is on a Stribeck curve. The coefficient of friction (CoF) is plotted against the Sommerfeld number.²³ Although classically the Stribeck curve was developed for analysis of bearing contacts between two cylinders, the idea has been used by some authors as a tool for the analysis of CMP friction measurements [e.g. (Refs. 24, 25)]. These two nondimensional numbers are defined as

$$\begin{aligned} \text{CoF} &= \frac{\bar{F}}{P\pi(D/2)^2} \\ \text{So} &= \frac{v\mu}{Ph} \end{aligned} \quad [3]$$

where \bar{F} is the average lateral force, determined from experiments, P is the applied normal pressure created by the externally applied downforce, as given in Table I, $D=180\text{ }\mu\text{m}$ is the diameter of the entire structure (including the post top and the 50 μm wide moat), v is the pad-wafer relative lateral velocity as given in Table I, μ is the slurry viscosity, taken to be 0.0018 Pa·s,¹⁸ and h is the slurry film thickness, estimated at 50 μm based on the work of Gray, et al.^{11,19} The estimate of the fluid film thickness is the least certain of the parameters. The results are shown in Fig. 14.

For all three experiments, the local CoF is larger than 1, indicating that the average lateral force on the post is larger than the average downward pressure. This is possible, since the asperities are catching on the edge of the post. The lateral force is expected to be

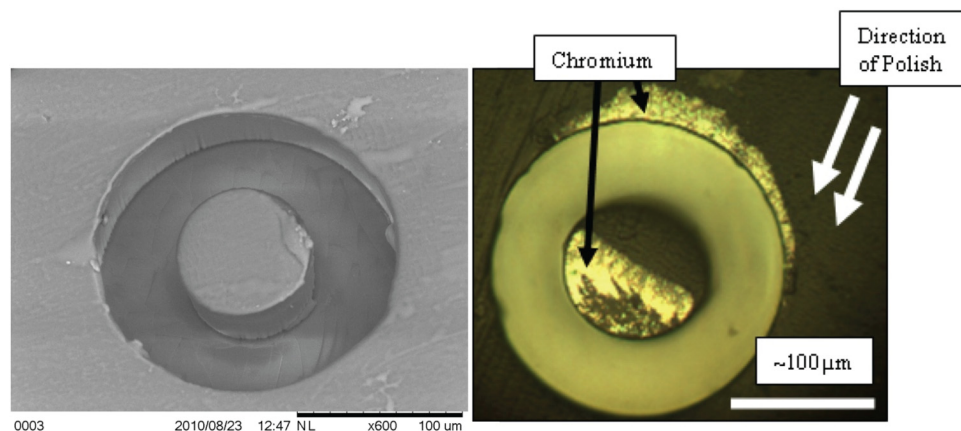


Figure 12. (Color online) Images of two posts after all polishing experiments are complete. (Left) Scanning electron microscope image showing that the PDMS structure is intact and no significant residue is left in the well. (Right) Light microscope image showing that the chromium is preferentially polished off the leading edge of the post top as well as the majority of the flat PDMS surface surrounding the post.

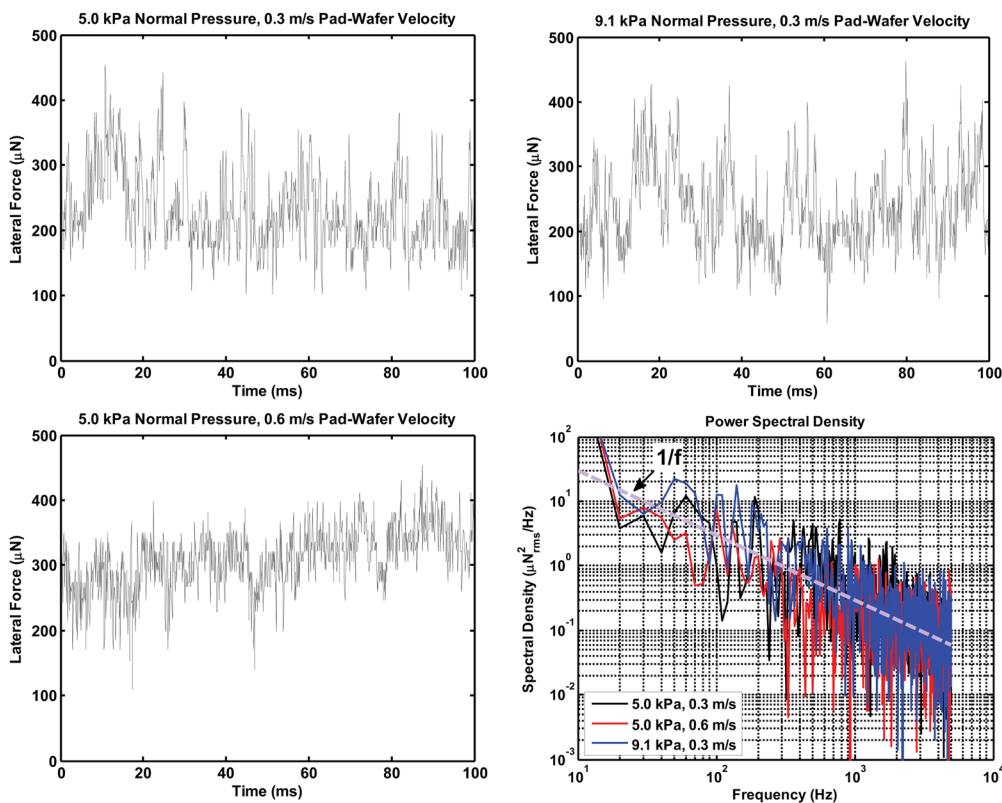


Figure 13. (Color online) Raw time domain data and power spectra for the three polishing cases. In the power spectra, the $(1/f)^1$ line is shown. In the first and last case this is a good fit to the data, but in the middle case, the data is best fit by $(1/f)^{0.56}$.

larger at structure edges than it would be on the featureless surface in between structures. This results in a local CoF that is larger than the global average CoF. The global average CoF for polishing a glass wafer in this experimental setup with a similar pad, slurry, downforce, and velocity is on the order of 0.5.⁴

The Sommerfeld numbers for the cases examined here are very small, less than 5×10^{-3} . This suggests that polishing operates in the solid-contact lubrication regime. The rising CoF with So is mildly surprising, therefore, as in the solid-contact regime, CoF is expected to be constant with So. It seems likely that in fact we are in a solid-contact lubrication regime where most of the normal contact force is transmitted via solid-solid contact. However, the complex nature of the inter-

actions between the pad and the PDMS post structure may produce a rising CoF which does not follow a typical Stribeck curve. A second possibility is that the fluid film thickness changes with downforce. In these computations, the fluid film thickness has been held fixed.

Dynamic model of contact

In order to explain the dynamic behavior of the structure in response to asperity contact forces, a dynamic model has been developed, shown in Fig. 15. We assume that only quasistatic motion and the first eigenmode of vibration are significant, which is justified due to the relatively high (25 kHz predicted) fluid loaded resonant frequency of the PDMS post, and the expectation that the forcing from asperity contacts will be primarily at 10 kHz and below. Under these assumptions, the dynamic model of the post is a second order system, driven by a time series of asperity contacts

$$\ddot{x} + 2\zeta\omega_n\dot{x} + \omega_n^2x = \frac{\omega_n^2}{k}F(t) \quad [4]$$

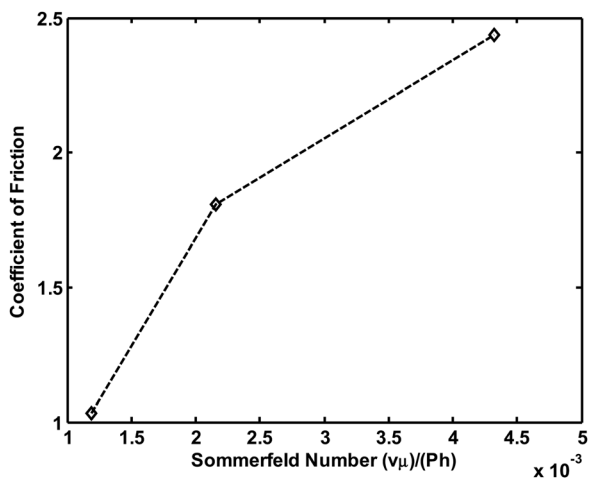


Figure 14. Stribeck curve comparing the local Coefficient of Friction to the Sommerfeld number.

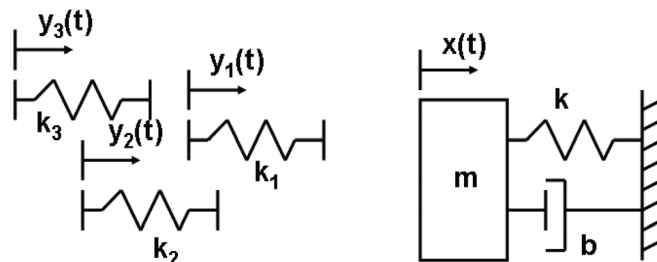


Figure 15. Dynamic model of post/asperity interaction. The post is modeled as a second order mass-spring-damper system, and the asperities are modeled as moving springs.

Table I. Time averaged results for the three polishing cases.

Mean pad/wafer normal load(kPa)	Mean pad/wafer relative velocity(m/s)	Mean lateral force(μ N)	RMS deviation of force about mean(μ N)	Power spectrum slope above 100 Hz(1/f)N
5.0	0.3	230	58	N = 0.95
5.0	0.6	210	47	N = 0.56
9.1	0.3	240	64	N = 1.0

where x is the deflection of the post top, ζ is the nondimensional damping ratio, ω_n is the undamped natural frequency of the structure, and k is the static tip stiffness of the structure. The static stiffness is taken to be $k = 8.3$ N/m, based on the static FEA analysis shown above and static calibration results presented later in the paper. The natural frequency of the post structure is taken to be $\omega_n = 2\pi(25$ kHz) based on the fluid loaded natural frequency predicted by Kirstein. The damping ratio for the structure is unknown; damping phenomena include viscous losses in the fluid, structural damping within the PDMS post, and structural damping in the asperities and contact regions. In the absence of any information in this regard, the damping ratio is selected to be $\zeta = 1$, a critically damped structure. Neither ω_n nor ζ have a significant impact on simulation results, as the majority of the forcing is occurring at frequencies below resonance.

$F(t)$ is the forcing function from asperity contacts, which can be written as the sum of contact forces from all N asperities which may at some time come into contact with the post

$$F(t) = \sum_{n=1}^N F_n(t) \quad [5]$$

The asperities are modeled as springs. The base of the asperity spring is attached to the rotating pad. Hence the force applied to the post is the relative position of the asperity base and the post top multiplied by the asperity spring constant. Before the asperity reaches the post, the force is zero. Once the force reaches some threshold value, the asperity is expected to slip off of the post and no longer contribute force. This can be expressed as

$$F_n(t) = \begin{cases} 0 & y_n(t) < x(t) \\ k_n(y_n(t) - x(t)) & y_n(t) \geq x(t) \text{ and } F_n(t) < F_{slip} \\ 0 & k_n(y_n(t) - x(t)) \geq F_{slip} \end{cases} \quad [6]$$

The positions of the asperities relative to the post top are equal to some randomly assigned initial position plus the motion due to the fixed pad velocity

$$y_n(t) = y_n(t=0) + vt \quad [7]$$

The statistics of the asperity initial position are determined based on the average number of asperity contacts per unit area, N_a . It is assumed that the asperities are uniformly distributed over the pad. If a time domain simulation of duration T is conducted, N asperities will be required. The post sweeps out an area of pad equal to the post diameter, D , times the pad displacement which occurs over the duration of the simulation, vT . Hence, $N = N_a DvT$. In the simulation, therefore, N asperities are used with initial positions uniformly distributed over the range $[-vT, 0]$.

Little is known about the statistics of the effective spring constants of the asperities. As a starting point, we assume that the spring stiffnesses of the N asperities are normally distributed with a mean of \bar{k}_n , and a standard deviation equal to one third of the mean, $\sigma = \bar{k}_n/3$. The standard deviation is chosen so that 99.9% of the asperity stiffnesses will fall between zero and twice the mean. The distribution is truncated at $k_n = 0$ so that no asperities have a negative stiffness.

The average force, RMS force, and the frequency spectrum of the force are all influenced by the number of asperity contacts, their average stiffness, and the slipping force. The power spectral density of the force in $\mu\text{N}^2/\text{Hz}$ is fit with a power law of the form $(1/f)^N$. Four parameters are varied in the model: F_{slip} , \bar{k}_n , N_a , and v . We consider three outputs from the model: average inferred force, the RMS deviation of the inferred force about the mean, and the exponent for the slope of the spectral density with frequency.

Simulations were run for a variety of cases, as detailed in Table II. In all cases the post structure properties were kept constant, equal to those for the actual structure under investigation. The parameters related to pad contact were varied over the ranges as shown. Every permutation of these parameters was run in a parallel computing environment, always using a total simulation time of 0.1 s and a simulation time step of 10 μs . An adaptive 4th/5th order Runge Kutta solver was used in Matlab. This resulted in 1008 simulation runs, from which the average post deflection, RMS post deflection, and power spectrum exponent were extracted. The results are plotted in a nondimensional form in Fig. 16. The average quasistatic lateral force normalized to the slipping force can be evaluated analytically, and is used as the abscissa for all three plots.

From the simulation results, we see that the majority of the simulation results lie along the curves, as determined using a least squares fit in log-log coordinates

$$\begin{aligned} \frac{F_{avg}}{F_{slip}} &= \frac{N_a D F_{slip}}{2k_{eff}} \\ \frac{F_{rms}}{F_{slip}} &= \frac{4}{5} \left(\frac{N_a D F_{slip}}{2k_{eff}} \right)^{1/2} \quad \text{for} \quad \frac{N_a D F_{slip}}{2k_{eff}} < 10 \end{aligned} \quad [8]$$

where k_{eff} is the effective series combination of the average asperity stiffness and the post stiffness

$$k_{eff} = k\bar{k}_n/(k + \bar{k}_n) \quad [9]$$

The last plot in Fig. 16 gives the exponent, N , for a best fit to the power spectra slope verses frequency, $(1/f)^N$, where the spectrum is in $\mu\text{N}/\text{Hz}^2$ units. These results show a maximum of $N = 2$ for most large values of the controlling parameter, but do not collapse onto a single curve at lower values.

Table II. Parameters used for dynamic simulation runs.

N_a (1/mm ²)	v (m/s)	\bar{k}_n (N/m)	F_{slip} (μ N)	k (N/m)	f_n (kHz)	ζ	D (μm)
10, 70, 100, 500, 1000, 5000, 10000	0.3, 0.6	0.001, 0.0032, 0.01, 0.032, 0.1, 0.32, 1, 3.2, 10	1, 2.7, 7.2, 19.3, 51.8, 139, 373, 1000	8.3	25	1	80

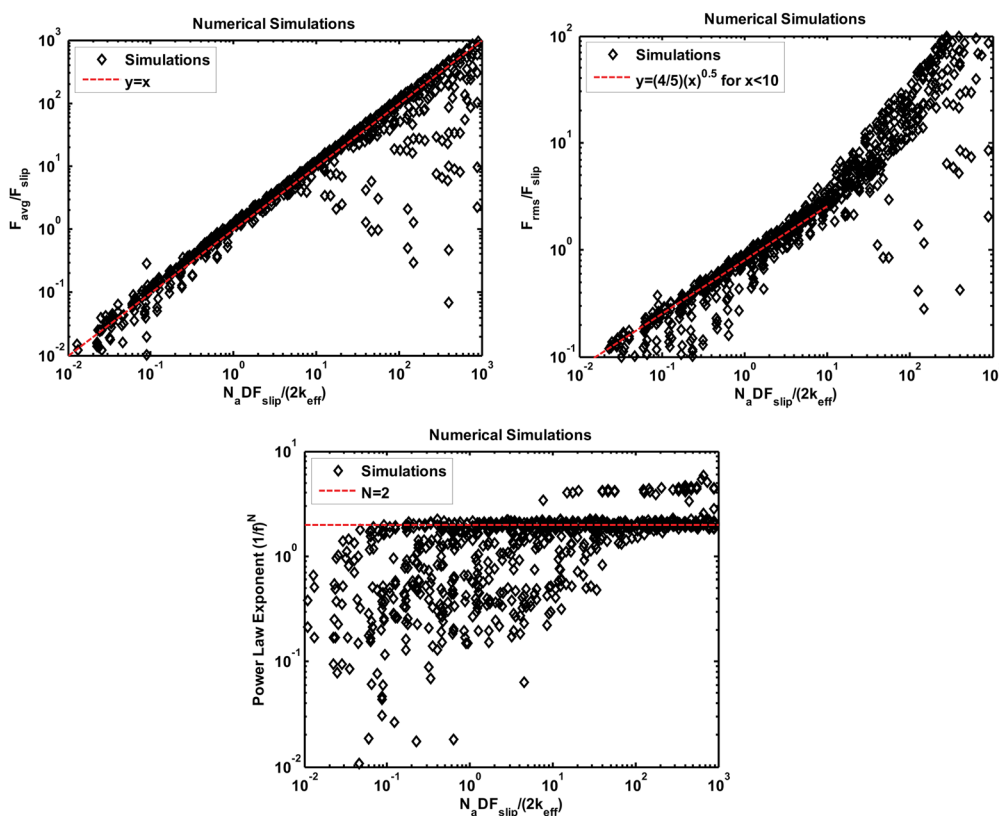


Figure 16. (Color online) Results of the 1008 simulation runs presented in log-log format. The average inferred force, RMS inferred force, and power spectra slope vs. frequency are all given in nondimensional form, as a function of the controlling parameter $N_a D F_{slip} / (2k_{eff})$.

If we can measure the resultant parameters F_{avg} , F_{rms} , and N , and if we know the test structure and process conditions, k , v , and D , then we can infer the microscale contact properties for the pad. That is, we can infer the number of asperity contacts per unit area, N_a , the slipping force, F_{slip} , the average asperity stiffness, \bar{k}_n .

The reader may note that the applied downforce during polishing does not enter explicitly into the simulation. However, downforce is implicitly involved because it changes the number of asperity contacts per unit area, N_a , the slipping force, F_{slip} and the effective asperity stiffness, \bar{k}_n .

Discussion

Using the results of Fig. 16 and the measured force data described in Table I, it is possible to estimate the unknown model parameters F_{slip} , \bar{k}_n , and N_a for the experimental cases. The results are given in Table III. In order to systematically evaluate the goodness of fit between the experimental data and the simulation, the following fitness function is minimized

$$g(F_{rms}, F_{avg}, N) = \left(\frac{F_{rms}^{sim}}{F_{rms}^{exp}} - 1 \right)^2 + \left(\frac{F_{avg}^{sim}}{F_{avg}^{exp}} - 1 \right)^2 + \left(\frac{N^{sim}}{N^{exp}} - 1 \right)^2 \quad [10]$$

For all three experimental results, the best fit amongst all 1008 simulation runs is for the parameter set $N_a = 5000 \text{ contacts/mm}^2$, $\bar{k}_n = 0.32 \text{ N/m}$, $F_{slip} = 19.3 \mu\text{N}$. It is important to note that this set of conditions is the optimal set of conditions, in the sense of minimizing equation (10), for both the $v = 0.3 \text{ m/s}$ and $v = 0.6 \text{ m/s}$ simulations. In the two simulation cases, as in the two experimental cases, the primary effect of doubling the velocity is a reduction in the slope of the PSD from approximately $(1/f)^1$ to $(1/f)^{0.6}$. In simulation, increasing the velocity also leads to a rise in average force and a slight reduction in RMS force, in agreement with experiment. The effects are somewhat more pronounced in the experimental data, however. Table III shows a comparison between the experimentally measured and simulated results for the two cases. Fig. 17 shows the time domain results and the power spectra.

The average asperity stiffness of $\bar{k}_n = 0.32 \text{ N/m}$ determined using this method is approximately 25 times more compliant than the PDMS post. Both structures are made of soft polymers and have similar dimensions, so it is plausible that they have a similar compliance, but no independent verification of pad asperity stiffness is available. The slipping force coupled with the average asperity stiffness suggests that the contact slips off when the post has deflected by $60 \mu\text{m}$. This deflection is approximately equal to the open region around the post, so it may be that the asperity slips off when the post touches the sidewall.

Table III. Simulated conditions compared to experimentally measured values.

Process conditions		Experimental measurements			Simulated conditions		
Normal load(kPa)	v(m/s)	$F^{avg}(\mu\text{N})$	$F^{rms}(\mu\text{N})$	N	$F^{avg}(\mu\text{N})$	$F^{rms}(\mu\text{N})$	N
5.0	0.3	230	58	0.95	297	60.6	1.01
5.0	0.6	310	47	0.56	311	60.0	0.60
9.1	0.3	240	64	1.0	297	60.6	1.01

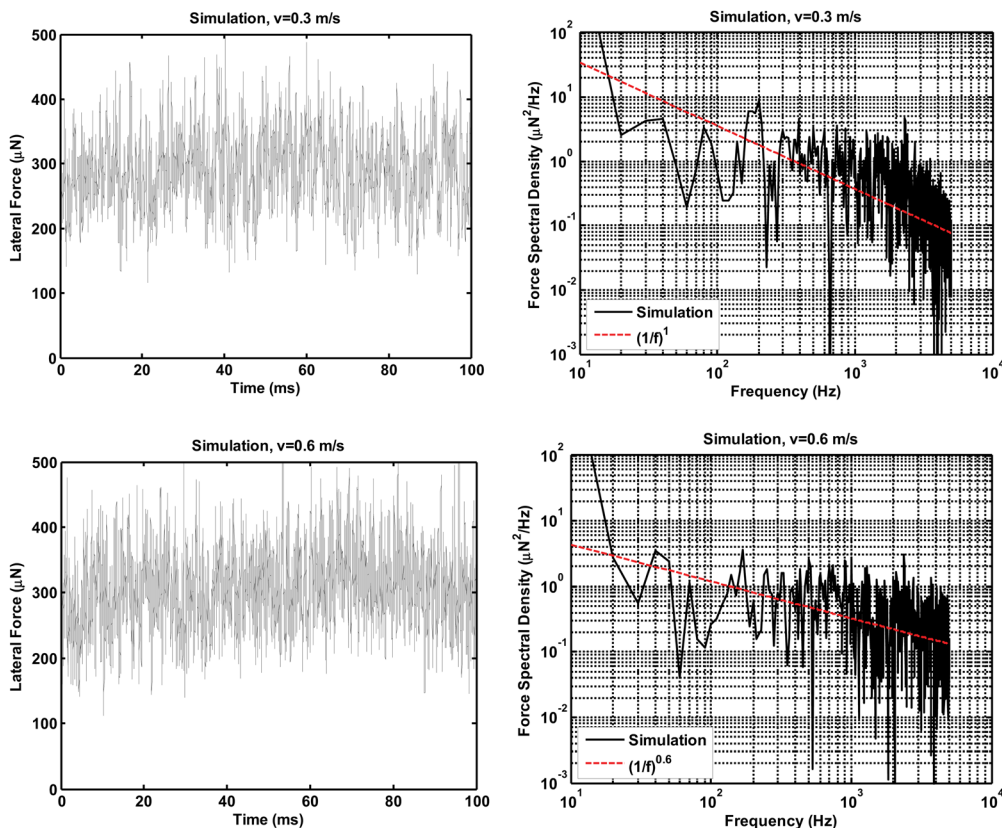


Figure 17. (Color online) The two simulation runs which are most similar to the experimental results. $F_{\text{slip}} = 19.3 \mu\text{N}$, $k_n = 0.32 \text{ N/m}$, $N_a = 5000 \text{ contacts/mm}^2$. (Left) Time domain results for the effective lateral force on the post tip. (Right) Power spectral density with a best fit power law. Two simulation cases are shown: one for $v = 0.3 \text{ m/s}$ and one for $v = 0.6 \text{ m/s}$. The average force, RMS force and exponent for these two cases are given in Table III.

The most interesting result is the number of contacts per unit area. Based on estimates from confocal microscopy for a static case,¹³ only approximately 70 contacts per mm^2 were expected. Yet the dynamic model applied here suggests approximately 5000 contacts per mm^2 . It may be that the confocal microscopy technique is missing many small contacts. Alternatively, it may be that in the dynamic case there truly are a larger number of contacts than in the static case. There are other significant differences between the two situations as well, including the type of wafer and pad, which play an important role in the nature of the contact. At present, we can conclude that large numbers (on the order of 5000 per mm^2) of contact points are present, and that the number of contacts does not vary strongly with downforce or velocity for the conditions described here. We also suspect that the nature of contact will be strongly influenced by pad and substrate type, although more evidence is needed to verify this conjecture.

Conclusions

A method for measuring the microscale contact forces between a polishing pad and a surface during CMP has been demonstrated. During polishing, for the experimental conditions described above, the averaged lateral contact force on an 80 micrometer diameter post top was between 230 and 310 μN . The RMS deviation of the force about the mean falls between 47 and 64 μN . Faster polishing cases show a 30% higher mean force, and a 20% reduction in the RMS variation of force about the mean. Little change is seen in the lateral force characteristics when increasing downforce. The power spectral density of the lateral force exhibits a $(1/f)^N$ character. The exponent N is found to vary strongly with the pad-wafer velocity, changing from 1.0 at 3 m/s to 0.6 at 0.6 m/s in both experiment and simulation. The measurement method has been coupled to a

simple dynamic model of asperity contact which can be used to extract approximate pad properties from the data. The method has been applied to the experimental case above and suggests an average asperity lateral stiffness of 0.32 N/m, on the order of 5000 asperity contacts per square millimeter, and a slipping force of 19.3 μN .

References

1. N. Mueller, C. Rogers, P. Manno, R. White, and M. Moynour, *J. Electrochem. Soc.*, **156**, H908 (2009).
2. J. Vlahakis, C. Rogers, V. P. Manno, R. White, M. Moynour, D. Hooper, and S. Anjur, *J. Electrochem. Soc.*, **156**, H794 (2009).
3. R. White, J. Vlahakis, C. Gray, V. Manno, N. Braun, D. Gauthier, A. Mueller, C. Rogers, and M. Moynour, In Situ Characterization of the Mechanical Aspects of CMP, in *International Conference on Planarization/CMP Technology*, Hsinchu, Taiwan (2008).
4. J. Vlahakis, V. P. Manno, C. B. Rogers, and R. White, *Electrochem. Solid-State Lett.*, **13**, H206 (2010).
5. L. M. Cook, *J. Non-Cryst. Solids*, **120**, 152 (1990).
6. E. Paul, *J. Electrochem. Soc.*, **148**, G355 (2001).
7. E. Paul, F. Kaufman, V. Brusic, J. Zhang, F. Sun, and R. Vacassy, *J. Electrochem. Soc.*, **152**, G322 (2005).
8. J. Lu, C. Rogers, V. P. Manno, A. Philipossian, S. Anjur, and M. Moynour, *J. Electrochem. Soc.*, **151**, G241 (2004).
9. Y. Sampurno, L. Borucki, and A. Philipossian, *J. Electrochem. Soc.*, **152**, G841 (2005).
10. E. J. Terrell and C. F. Higgs Iii, *J. Electrochem. Soc.*, **153**, K15 (2006).
11. C. Gray, C. Rogers, V. P. Manno, R. White, M. Moynour, and S. Anjur, Determining Pad-Wafer Contact Using Dual Emission Laser Induced Fluorescence, Materials Research Society, Warrendale, Pa (2007).
12. C. Gray, R. White, V. P. Manno, and C. B. Rogers, *Tribol. Lett.*, **29**, 185 (2008).
13. C. L. Elmudidi and G. P. Muldowney, A Novel Optical Technique to Measure Pad-Wafer Contact Area in Chemical Mechanical Planarization, Materials Research Society, 506 Keystone Drive, Warrendale, PA (2006).
14. G. B. Basim, I. U. Vakarelski, and B. M. Moudgil, *J. Colloid Interface Sci.*, **263**, 506 (2003).

15. A. Feiler, I. Larson, P. Jenkins, and P. Attard, *Langmuir*, **16**, 10269 (2000).
16. D. Armani, C. Liu, and N. Aluru, *Re-configurable fluid circuits by PDMS elastomer micromachining*. IEEE Conference on Microelectromechanical Systems, MEMS '99, 1999.
17. S. Kirstein, M. Mertesdorf, and M. Schonhoff, *J. Appl. Phys.*, **84**, 1782 (1998).
18. W. Lortz, F. Menzel, R. Brandes, F. Klaessig, T. Knothe, and T. Shibasaki, *News from the M in CMP-Viscosity of CMP Slurries, A Constant?*, Materials Research Society, Warrendale, Pa (2003).
19. C. Gray, *Detecting Pad-Wafer Contact in CMP using Dual Emission Laser Induced Fluorescence*, Tufts University, Medford (2008).
20. Y. N. Xia and G. M. Whitesides, *Ann. Rev. Mater. Sci.*, **28**, 153 (1998).
21. M. Hopcroft, T. Kramer, G. Kim, K. Takashima, Y. Higo, D. Moore, and J. Brugger, *Fatigue Fract. Eng. Mater. Struct.*, **28**, 735 (2005).
22. A. M. Scarfo, V. P. Manno, C. B. Rogers, S. P. Anjur, and M. Moinpour, *J. Electrochem. Soc.*, **152**, G477 (2005).
23. H. W. Swift, General discussion on lubrication and lubricants: Group I. Journal and thrust bearings. ARCHIVE: Proceedings of the Institution of Mechanical Engineers 1847-1982 p. 121 (1937).
24. A. Philipossian and S. Olsen. Effect of pad surface texture and slurry abrasive concentration on tribological and kinetic attributes of ILD CMP, in *Mater. Res. Soc. Symposium*, Materials Research Society (2003).
25. P. B. Zantye, A. Kumar, and A. K. Sikder, *Mater. Sci. Eng. R*, **45**, 89 (2004).